

Small-Angle X-ray Scattering: Characterization of cubic Au nanoparticles using Debye's scattering formula

Jérôme Deumer^{*})

Physikalisch-Technische Bundesanstalt (PTB), Abbestr. 2-12, 10587 Berlin, Germany

Brian R. Pauw^{†)}

Federal Institute for Materials Research and Testing (BAM), Unter den Eichen 87, 12205 Berlin, Germany

Sylvie Marguet^{‡)}

Université Paris-Saclay, CEA, CNRS, NIMBE, 91191 Gif-sur-Yvette, France

Dieter Skroblin^{§)}

Physikalisch-Technische Bundesanstalt (PTB), Abbestr. 2-12, 10587 Berlin, Germany

Olivier Taché^{¶)}

Université Paris-Saclay, CEA, CNRS, NIMBE, 91191 Gif-sur-Yvette, France

Michael Krumrey^{||)}

Physikalisch-Technische Bundesanstalt (PTB), Abbestr. 2-12, 10587 Berlin, Germany

Christian Gollwitzer^{**)}

Physikalisch-Technische Bundesanstalt (PTB), Abbestr. 2-12, 10587 Berlin, Germany

(Dated: May 2, 2022)

We propose a versatile, user-friendly approach, named (Computing Debye's scattering formula for Extraordinary Formfactors) (**CDEF**), to approximately calculate scattering profiles of arbitrarily shaped nanoparticles for small-angle X-ray scattering (SAXS) using Debye's scattering formula, also known as the Debye equation. This equation generally allows to compute the scattering pattern of an ensemble of scatterers with a known form factor in the kinematic limit. The ensemble can hereby consist of atoms, atomic nuclei or larger shapes. In the method proposed in this paper, a quasi-randomly distributed point cloud in the desired particle shape is generated. Then, Debye's formula is applied to this ensemble of point scatterers to calculate the SAXS pattern of a single particle with random orientation. The quasi-random distribution ensures faster convergence compared to a true random distribution of scatterers, especially in the higher region of the momentum transfer q . In order to compute realistic SAXS curves of polydisperse nanoparticle ensembles with a given size distribution, the single particle master curve is rescaled and convolved with the size distribution. This allows us to fit measured data in reasonable time.

We have used the method to evaluate scattering data of Au nanocubes with truncated or rounded edges, which were measured at the four-crystal monochromator beamline of PTB at the synchrotron radiation facility BESSY II in Berlin. Our implementation of this method is fast enough to run on a single desktop computer and perform model fits within minutes. The accuracy of the method was analyzed by comparison with analytically known form factors and another implementation, the SPONGE, based on a similar principle but with fewer assumptions. Additionally, the SPONGE coupled to McSAS3 allows us to further retrieve information on the uncertainty of the size distribution using a Monte-Carlo uncertainty estimation algorithm.

Keywords: SAXS, Debye's scattering formula, non-spherical nanoparticles

I. INTRODUCTION

Small-angle X-ray scattering (SAXS) is a powerful nanostructure quantification tool to characterize ensembles of nanoparticles^{1,2}. X-ray scattering patterns principally contain information on the sample's pair-distance distribution, which can be interpreted to obtain e.g. the particles' shape, size distribution, number concentration,

specific surface area, or radius of gyration¹⁻⁶. It is a non-destructive method with only little sample preparation for particles in liquid suspension, and also applicable for powders and porous materials⁷. With SAXS, typically particles with sizes ranging from a few nanometers up to a few hundred nanometers can be measured, if there is sufficient electron density contrast of the par-

ticles relative to the suspension medium, since photons are scattered by the electrons in the material. The higher the electron density contrast, the more pronounced the scattered intensity relative to the background signal originating from the suspension. The measured SAXS signal can be further processed and fitted to gain information about the desired particle properties.

In order to fit and evaluate experimental data, an adequate assumption of the underlying particle shape is necessary. This assumption is made by choosing the correct form factor F for the physical model. F as a function of the photon's momentum transfer \vec{q} is defined by Fourier transformation of the particle's electron density contrast $\Delta\rho$:²

$$F(\vec{q}) = \int_V dV \Delta\rho(\vec{r}) \exp -i\vec{q} \cdot \vec{r}. \quad (1)$$

For simple particle shapes such as spheres, cylinders or spherical core-shell particles, F can be calculated analytically³. For instance, F of a perfect sphere with a homogeneous electron contrast $\Delta\rho$ is well known as¹⁻³

$$F_{sph}(q, R, \Delta\rho) = \Delta\rho \left(\frac{4}{3}\pi R^3 \right) \left(3 \frac{\sin qR - qR \cos qR}{(qR)^3} \right), \quad (2)$$

where R is the radius of the sphere and q is the modulus of momentum transfer of the scattered photons. Since F generally represents the amplitude of the scattered radiation for a certain direction of \vec{q} , the corresponding scattering profile of a dilute nanoparticle ensemble can be obtained as

$$I(q, R, \Delta\rho) = \langle |F(\vec{q}, R, \Delta\rho)|^2 \rangle_{\Omega}, \quad (3)$$

with $\langle \cdot \rangle_{\Omega}$ being the particles' orientation average which originates from the isotropic alignment of the particles within the ensemble.

Besides equation (2), several other analytic expressions of F exist for other shapes with spherical symmetry such as single shells, core-shell spheres, or multiple concentric shells^{3,8,9}. Analytic expressions of F also exist for regular shapes with lower symmetry such as ellipsoids⁸, cylinders^{3,10} and for cylindrical and conical shaped particles with an arbitrary polygonal base which are built out of polygonal wedges¹¹. The particle shapes with spherical symmetry have in common that calculating $\langle \cdot \rangle_{\Omega}$ is trivial whereas for all non-spherical particles such as cylinders^{3,10}, ellipsoids⁸, or cubic particles⁸ averaging $|F(\vec{q})|^2$ numerically over all possible particle orientations is necessary, leading to higher computational effort. In general, spherical averaging is done by calculating

$$\langle |F(\vec{q})|^2 \rangle_{\Omega} = \frac{1}{4\pi} \int_0^{2\pi} d\phi \int_0^{\frac{\pi}{2}} d\theta \sin \theta |F(q, \phi, \theta)|^2, \quad (4)$$

where variables ϕ and θ describe angles between \vec{q} and specific rotational symmetry axes of the particularly

shaped particle. For particles with one axis of rotational symmetry such as cylinders, a one-dimensional numerical average is sufficient, meaning F in case of cylindrical particles would not depend on ϕ as defined in equation (4). For cubic shaped particles, however, spherical averaging must be carried out over two independent coordinates^{8,12}. This will become relevant when calculating a whole scattering curve $I(q)$ at several thousand values of q , and especially when fitting experimental data.

Recently, a seemingly limitless landscape of nanomaterial shapes and structures has been synthesized that do not fit these analytical functions such as stars, cubes with concave faces or core-shell-structured cubes^{13,14,15} demanding for a convenient method of calculating scattering profiles $I(q)$ of these complex shaped particles. Widespread SAXS analysis software such as *SASfit*^{3,16} or *SasView*¹⁷ use extended libraries of analytic expressions of F to evaluate SAXS data, however, analytic solutions of F regarding more complex-shaped particles may not be available to the complexity of solving equation (1), which can quickly become intractable¹¹.

With the present paper, we want to introduce our new CDEF which enables us to numerically calculate isotropic scattering profiles $I(q)$ of polydisperse ensembles of arbitrarily shaped nanoparticles, and eventually use it to evaluate the size distribution of synthesized Au nanocubes (section III). The results are then compared with those using the already existing program called the SPONGE. Both methods use the Debye equation in slightly different ways, whereas the SPONGE serves as a reference method since it has already proven to deliver reliable results¹⁸. For this introduction, the methodology of both methods will be explained in section II followed by technical and experimental details in section IV, whereas in section III general information about the synthesized nanocubes will be presented. Finally, section V will then discuss the results in detail.

II. METHODS

In this section, CDEF as well as the SPONGE will be described in more detail. Both methods use Debye's scattering formula (eq. (6)) to approximately calculate $I(q)$ for arbitrarily shaped nanoparticles. In doing so, Debye's scattering formula is applied onto a three dimensional (3D) point cloud of the desired particle shape. The point cloud is created by generating a 3D triangle mesh of the associated particle shape first and then randomly filling it with punctiform scatterers to approximate a corresponding particle with a homogeneous density $\Delta\rho$. Similar approaches of using Debye's scattering formula have been mentioned by G. Porod², J. S. Pedersen⁸ or S. Hansen¹⁹ in the context of spherical scatterers, however, Debye's formula can be implemented in many modified ways, influencing the accuracy of calculations as well as the ease of use.

In terms of Debye's scattering formula, $I(q)$ is expressed as a sum of the intensities scattered by each

individual scatterer plus interference terms due to the different spatial positions of the scatterers relative to one another. Hence, the q -dependence of $I(q)$ is influenced by the distance distribution of pairs of scatterers and their associated form factors, i.e. electron numbers in case of punctiform scatterers.

As a computing tool to performantly evaluate Debye's scattering formula CDEF uses an open-source software package called DEBYER²⁰ whereas the SPONGE uses its own implementation of the Debye equation (fig. 1).

II.A. Theory of Debye's scattering formula

In more general terms, Debye's scattering formula can also be used to calculate SAXS profiles of systems that consist of non-spherical sub-particles such as cylinders. In this case, the form factors of the sub-particles depend on their orientation w.r.t the momentum transfer \vec{q} which needs to be considered during the mathematical derivation². In this section, we focus on scatterers with a spherical or punctiform shape only². Arbitrarily shaped nanoparticles can subsequently be modelled as large systems of elementary punctiform scatterers where mainly the underlying distance distribution of scattering pairs determines the corresponding SAXS profile. The distance distribution of a 3D cloud of N scatterers is the probability distribution of the distances $|\vec{r}_{k,j}| = |\vec{r}_k - \vec{r}_j|$ of each corresponding pair of scattering points (\vec{r}_k, \vec{r}_j) .

Further descriptions of the following theoretical discussion can be found in various references^{2,20,21}. In the following, we assume coherent and elastic scattering of the incoming X-ray photons in the kinematic limit, meaning photons are only scattered once by the cloud's scatterers before being detected²². The scattered intensity at the detector can then be described as²¹

$$\begin{aligned} I(\vec{q}) &= \Psi(\vec{q})\Psi^*(\vec{q}) \\ &= \sum_{k=1}^N \sum_{j=1}^N f_k(\vec{q})f_j^*(\vec{q}) \exp(i\vec{q} \cdot \vec{r}_{k,j}), \end{aligned} \quad (5)$$

with Ψ being the cloud's complex-valued form factor where Ψ^* indicates the complex-conjugate of Ψ , f_k being the complex-valued form factor of a single scatterer with spatial position \vec{r}_k , and \vec{q} being the momentum transfer.

If we now assume an isotropic distribution of the particle orientation, the phase term in equation (5) can be averaged over a spherical surface with radius $r_{k,j}$ leading to Debye's scattering formula^{2,20,21,23}:

$$\begin{aligned} I(q) &= \sum_{k,j}^N |f|^2 \langle \exp i\vec{q} \cdot \vec{r}_{k,j} \rangle \\ &= |f|^2 \sum_{k,j}^N \frac{\sin qr_{k,j}}{qr_{k,j}}. \end{aligned} \quad (6)$$

For a better understanding of how the software DEBYER works, it is now convenient to rewrite eq. (6) as^{2,20}

$$\begin{aligned} I(q) &= |f|^2 \left(\sum_k^N \frac{\sin qr_{k,k}}{qr_{k,k}} + \sum_{k \neq j}^N \frac{\sin qr_{k,j}}{qr_{k,j}} \right) \\ &= |f|^2 \left(N + 2 \sum_k^N \sum_{k < j}^N \frac{\sin qr_{k,j}}{qr_{k,j}} \right). \end{aligned} \quad (7)$$

Again, introducing the number of pairs $n(r)$ with intra-pair distance r ,

$$n(r) = \sum_k \sum_{k < j} \delta(r - r_{k,j}), \quad (8)$$

yields the final result of Debye's scattering formula used by DEBYER²⁰:

$$\begin{aligned} I(q) &= |f|^2 \left(N + 2 \int_0^{+\infty} n(r) \frac{\sin qr}{qr} dr \right) \\ &\approx |f|^2 \left(N + 2 \sum_k^{N_{BINS}} n_k \frac{\sin qr_k}{qr_k} \right). \end{aligned} \quad (9)$$

Eq. 9 is obtained by binning the integral, thus n_k is the number of pairs of the k -th bin w. r. t. the intra-pair distance r_k . All in all, the basic concept of DEBYER's algorithm consists of calculating a rebinned histogram of the intra-pair distances of the 3D cloud with N_{BINS} bins. Thereafter, eq. 9 is applied to calculate the corresponding single-particle $I(q)$ ²⁰.

II.B. Implementation details of CDEF

With CDEF, respectively the SPONGE, we can additionally calculate polydisperse SAXS profiles. First the corresponding single-particle SAXS profile I_{MONO} is calculated as described above. Due to the assumed homogeneous electron density inside the particles, different particle sizes can be calculated by rescaling I_{MONO} . The quasi-random filling of scattering points is done using a scrambled Halton algorithm²⁴. The generated 3D point cloud is represented by a matrix in which each row represents the Euclidean coordinates of a single scatterer plus its real-valued electron number. This electron number can be adjusted to simulate different electron densities $\Delta\rho$. This matrix is then handed over to the open source software Debyer²⁰. Compared to a true-random particle filling, the quasi-random particle distribution of points enables us to sample the particle's volume more efficiently, meaning the projection of the points on each of the three coordinate planes is more uniform²⁴ (fig. 2). Hence, the modelled electron density is more homogeneous compared to the same number of points N in a random filling.

The SAXS curve of a polydisperse ensemble is then generated by integrating the form factor $F(q, R)$ of the assumed model over all particle sizes R with assumed size distribution $d(R; \sigma)$ giving

$$I_{\text{POLY}}(q) = \int_0^{\infty} d(R; \sigma) \underbrace{|F(q, R)|^2}_{I_{\text{MONO}}(q, R)} dR. \quad (10)$$

Eq. (10) can be approximated by a discrete sum of N_S rescaled single-particle SAXS curves I_{MONO} which are generated in accordance to $d(R; \sigma)$ such as

$$I_{\text{POLY}}(q) \approx \frac{1}{N_S} \left(\sum_{\{R_i | d(R; \sigma)\}} I_{\text{MONO}}(q, R_i) \right), \quad (11)$$

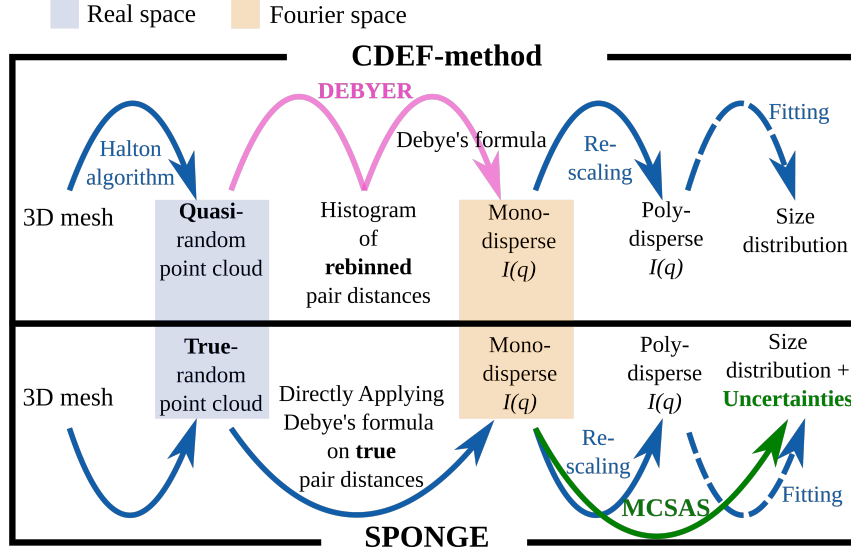


Figure 1 Comparison between CDEF and the SPONGE. Both methods use Debye's scattering formula to calculate the single-particle scattering profile starting from the associated three-dimensional (3D) mesh which represents the arbitrary particle shape.

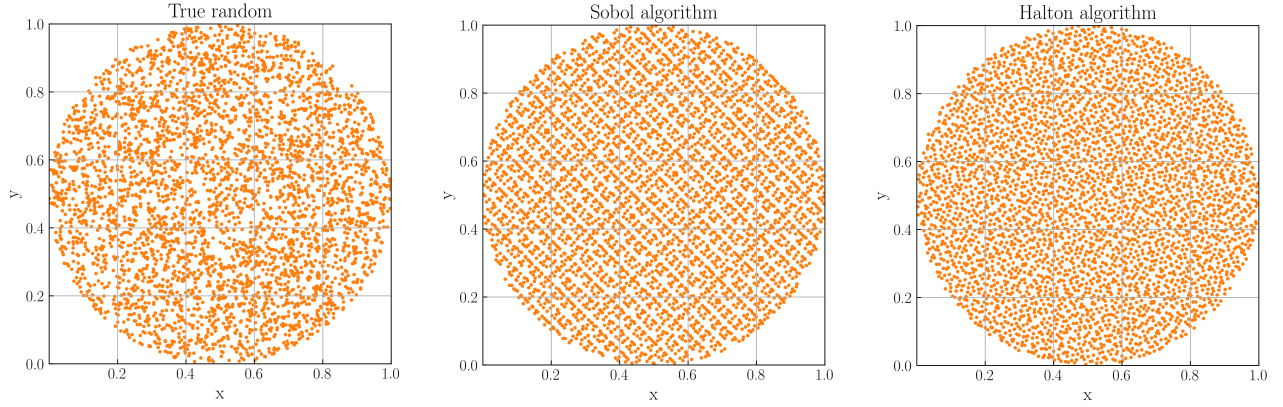


Figure 2 Examples of circular point clouds with radius $r = 0.5$ generated with one true-random and two quasi-random (Sobol, Halton) filling algorithms. Each cloud is generated by initially filling 5000 points into a squared area with side length $l = 1$ and subsequently deleting all points outside of the defined circle. Therefore each circle consists of a similar number of ~ 4.000 points. The usage of a quasi-random algorithm leads to a higher homogeneity of the spatial distribution relative to the true-random method whereas the true-random distribution shows a higher degree of local clustering.

where $(R; \sigma)$ is the number-weighted size distribution with standard deviation σ which is assumed to be Gaussian:

$$d(R; \sigma) = c_{\text{scaling}} \cdot (2\pi\sigma^2)^{-\frac{1}{2}} \exp -\frac{(r - R)^2}{2\sigma^2}, \quad (12)$$

normalized to unity with the scaling factor where the scaling factor causes c_{scaling} .

Rescaling the SAXS curve is straight-forward because the scattered intensity scales with the square of the particle's volume $V^2 \propto (R^3)^2$, and q scales with the inverse of the particle's radius $1/R$. The *radius* R here is a characteristic dimension of the shape like the radius in case of a sphere or the distance between two edges for more general shapes.

This procedure enables us to compute SAXS profiles of polydisperse ensembles with low computational effort for any given size distribution, and eventually to fit experimental data I_{EXP} by minimizing²⁵

$$\chi^2 = \frac{1}{N_q - M} \sum_i^{N_q} \left[\frac{I_{\text{EXP}}(q_i) - I_{\text{MOD}}(q_i)}{\sigma(I_{\text{EXP}}(q_i))} \right]^2. \quad (13)$$

Here, χ^2 is the reduced residual sum of squares of a model function I_{MOD} related to the experimental data at each measured data point q_i , N_q is the total number of data points and M is the number of used fit parameters²⁵.

I_{MOD} , moreover, is defined as

$$I_{\text{MOD}}(q, N_C, R, \sigma) = N_C I_{\text{POLY}}, \quad (14)$$

where N_C is a constant which is proportional to the number concentration C of the measured particle ensemble. If the measured intensity I_{EXP} is in absolute scattering units, then⁵:

$$C = \frac{N_C}{r_e^2 \cdot \Delta\rho^2}, \quad (15)$$

where $r_e \approx 2.82 \cdot 10^{-15}$ m is the classic electron radius.

II.C. CDEF vs. analytic formulae

As a validation of the introduced CDEF, we first compare its numerical results with the corresponding analytic form factors of common particle shapes using the three introduced filling algorithms (fig. 2). In this context, fig. 3 shows the analytically and numerically calculated single-particle SAXS profiles of a homogeneous sphere with radius $R = 10$ nm and electron contrast $\Delta\rho = 1 \text{ nm}^{-3}$. The analytic profile $I_{\text{Anal.}}$ was calculated by combining equation (2) and (3). It shows the well-known distinct oscillations with pronounced minima. The oscillations decrease with $\sim q^{-4}$ at higher q -values.

For the calculation of each numerical profile, spherical clouds were generated by first filling 30 000 points into a cubic bounding box with side length $2R = 20$ nm and then deleting all points outside of the defined sphere, which yields approximately $N \approx 30\,000 \cdot \pi/6 \approx 15\,700$ scattering points. This ratio must be taken into account in particular when comparing the absolute intensities I of the numeric profiles with each other since I depends on the sampled particle volume relative to the volume of the bounding box.

For the quasi-random fillings, we used the Sobol and Halton algorithms. As depicted in fig. 3, both quasi-random profiles match the analytic profile in good agreement up to the 7th local maximum, whereas at higher q -values both profiles start deviating from the analytic profile due to the artificial scattering signal originating from the clouds' fine structure. This also holds true for the true-random filling pattern with approximately the same number of scattering points, however, it only matches $I_{\text{Anal.}}$ up to the 4th local maximum due to a "scattering plateau" with an intensity value of $I \approx 10^3$. Thus, the overall usable q -range is greatly improved by the quasi-random filling algorithms, which is an advantage when aiming to evaluate the largest possible q -range, but at the same time keeping N as small as possible because computing time scales with N^2 . The less usable q -range of the true-random distribution results from the more pronounced local clustering of the distributed scattering points (compare fig. 2) leading to a wider distributed spectrum of the calculated intensity since both are related by Fourier transformation. On the other hand,

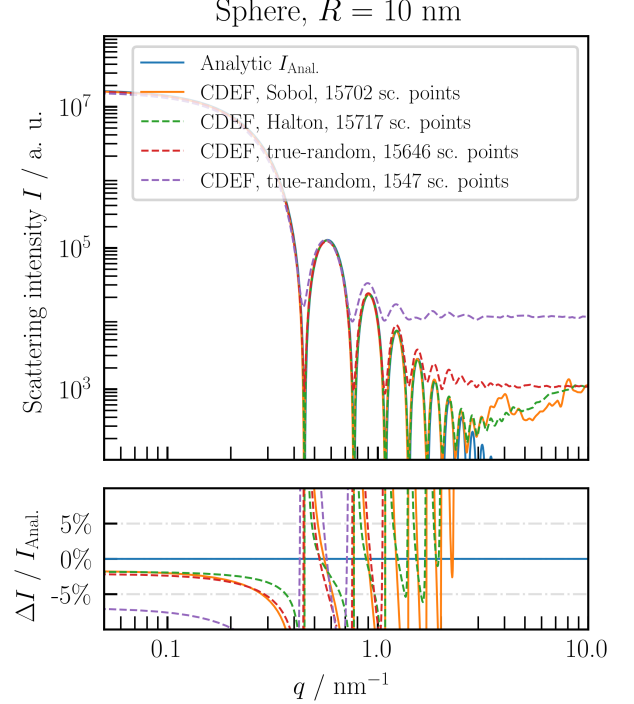


Figure 3 Comparison of simulated single-particle SAXS profiles using CDEF with the exact analytic SAXS profile $I_{\text{Anal.}}$ of a sphere with radius $R = 10$ nm and electron contrast $\Delta\rho = 1 \text{ nm}^{-3}$. For the numerical calculations, the Debye equation was applied on spherical clouds which were generated using two different quasi-random (Sobol, Halton) and one true-random filling algorithms. At specific q -values the artificial scattering signal from the fine structure of the individual cloud dominates the numeric profiles leading to a deviation from $I_{\text{Anal.}}$.

the quasi-random algorithms show less local clustering (a higher distance distribution) which results in smaller distributed artificial scattering signals manifesting only at higher values of q .

Fig. 3 also shows that using 10 times less scattering points lifts the scattering plateau of the true-random distributed SAXS profile such that only the first local maximum is matched adequately, whereas no difference is evident in the low q range. In general, a higher N shifts the usable range of this approximation to higher values of q , whereas the low q region is mostly unaffected.

In order to evaluate the performance of the method for particles with lower symmetry, figure 4 compares analytically and numerically obtained single-particle SAXS profiles of two cylinders with different aspect ratios L/R and $\Delta\rho = 1 \text{ nm}^{-3}$. The analytic SAXS curves were calculated using the well-known expression^{3,10}. For the calculation of each numerical profile, cylindrical clouds of $N \approx 30\,000 \pi/4 \approx 23\,560$ scattering points were generated similarly to the spherical clouds before. Regarding the cylinder with the lower aspect ratio, the quasi-random profiles match the analytic one up to the 5th local maximum, whereas the true-random pattern matches the analytic solution only up to the first local maximum.

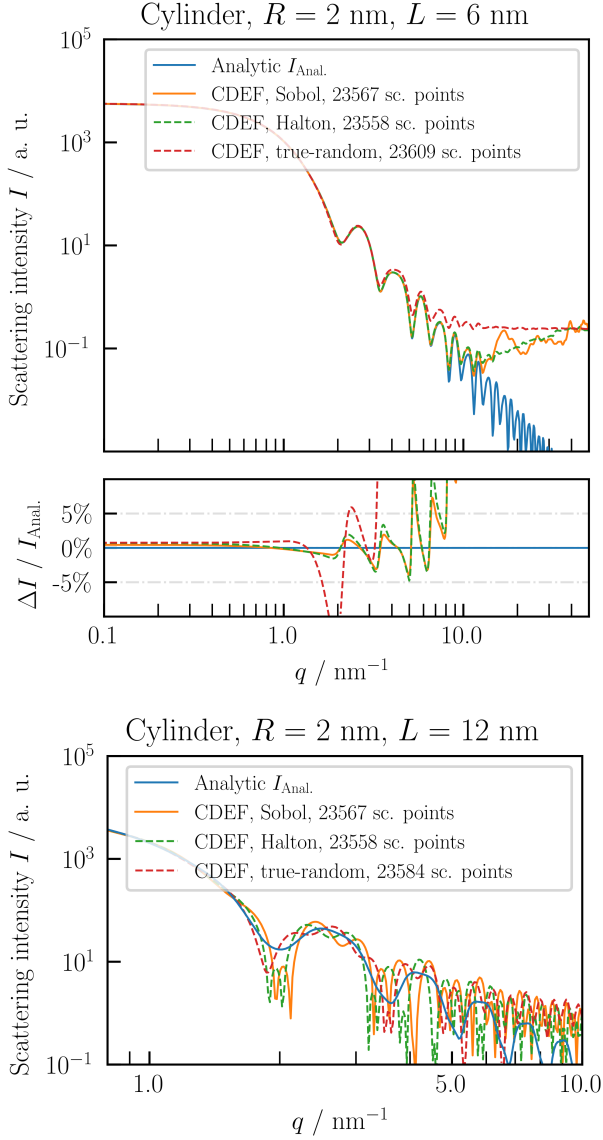


Figure 4 Comparison between numeric and analytic single-particle SAXS profiles of two different cylinders with radius R , length L and electron contrast $\Delta\rho = 1 \text{ nm}^{-3}$. At aspect ratios above ~ 4 the numeric scattering pattern using the Debye equation becomes noisy such that the oscillations of $I_{\text{Anal.}}$ cannot be matched.

Using CDEF with $N = 30\,000$ starting points, we could satisfactorily calculate SAXS profiles of cylinders up to aspect ratios of ~ 4 . Exceeding this ratio causes the calculated SAXS signal to become very noisy at higher q -values (fig. 4) making our method unsuitable for data analysis, even if the number of sub-scatterers is increased up to 100 000.

Regarding ideal cubes, CDEF is also able to adequately match $I_{\text{Anal.}}$ as depicted in figure 5. The analytic curve was calculated by averaging the expression from Ref¹² over two independent spatial coordinates. For this particular cube with side-to-side length 10 nm, CDEF with 30 000 scatterers as well as $I_{\text{Anal.}}$ were evaluated on 600 q -

values, whereas for each numeric profile CDEF was more than 25 times faster (33 s vs. 849 s).

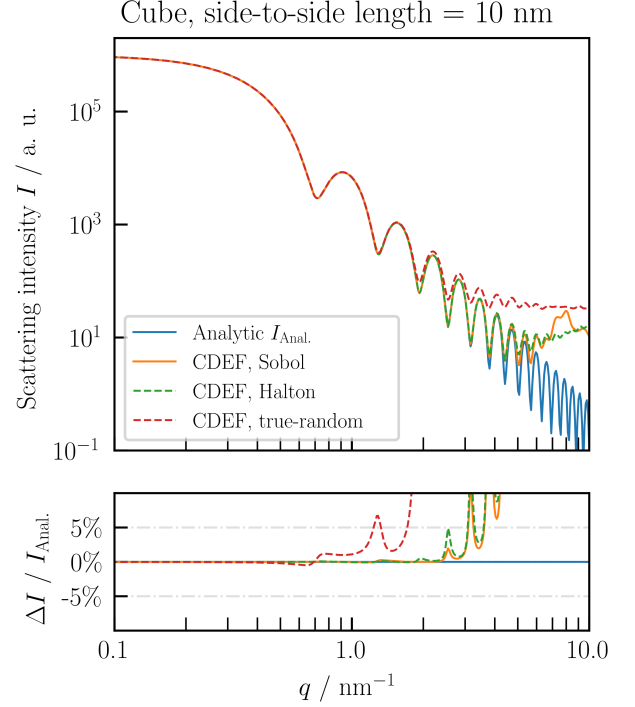


Figure 5 Comparison between numeric and analytic single-particle SAXS profiles of an ideal cube with side-to-side length 10 nm and electron contrast $\Delta\rho = 1 \text{ nm}^{-3}$.

II.D. SPONGE

II.D.1. Implementation details of the SPONGE

A separate implementation was developed, called the SPONGE, that is a more fundamentally proximate method by eschewing many of the speed-improving approximations. It uses the Debye equation for infinitesimally small point pairs as in equation (6), and uses a fully random point distribution. This method is similar to that presented by Hansen¹⁹, with the exception that the intermediate step where the numerical pair distance distribution function is generated, is bypassed in favor of a more direct approach, further minimizing potential sources of error.

While the SPONGE is much more computationally intensive, it should be more accurate over the entire q -range where the homogeneous phase approximation holds, and thus can be used to validate that the approximations in the faster CDEF implementations are not generating unforeseen artefacts. Like CDEF, the SPONGE uses the surface description in the STL format to define the boundaries of a nano-object. It then leverages the fast VTK bindings in Python for point placement, and determination whether the point lies inside or outside of the object. The computation of the point-

to-point Euclidian distance matrix is done using a fast SciPy implementation²⁶, before the Debye equation is applied to obtain a simulated isotropic scattering curve. By entering a scattering length density, the SPONGE-simulated data can be scaled to absolute units (i.e. to an absolute scattering cross-section in $1/\text{msr}$).

This procedure is then repeated, resulting in a number of independently generated scattering curves, each based on their own set of random points. The mean intensity from all repetitions is then presented, with the standard deviation used as an estimate for the uncertainty for each point.

A number-weighted size distribution can also be taken into account. The SPONGE currently implements a Gaussian size distribution, which is implemented by picking a random scaling factor for the q -vector for each independent repetition, and which affects the total intensity scaling factor based on its scaled volume (in a procedure identical to that as given in section II.B). This would be similar in reality to probing a multitude of objects of different size to build up the average scattering pattern. This size distribution has been verified to work accurately (by checking the result with a fit in SasView) up to a Gaussian distribution width σ of at least 50%. This simulated distribution width is not used for fitting, but is used to avoid unrealistically sharp minima in the simulated curve. For the simulations presented herein, the distribution width is set to 1%.

II.D.2. The SPONGE and MCSAS3

The thus simulated data of primary particles can be used to fit an experimental dataset, even when the experimental dataset is from a sample with an unknown, broader distribution of particle sizes. For this, we turn the simulated data into a fitting model for use with the Monte Carlo approach as implemented in McSAS^{27,28}. As the original McSAS is not easily adapted to support such a model description, we are here using the refactored McSAS3 implementation (currently in the last stages of development). McSAS3 works using the same methods as McSAS, but has many practical improvements such as multi-threaded optimization, a gui-independent backend (for headless computation), and the option to re-histogram a previous optimization run (McSAS on GitHub²⁹).

The simulated data can be converted into a fitting model, provided it has a Guinier region at low q , and (on average) a Porod region at high- q . Then, for a given scaling factor, the q vector of the simulated data is rescaled (in a manner identical to section III), and the intensity interpolated to the requested q vector of the experimental data. Datapoints that fall outside the limits of the simulated data are extrapolated using a flat (Guinier) approximation at low q , and a Porod slope at high q .

Using this fitting model in McSAS3, experimental data can be fitted rapidly using the simulated scattering pattern of an elementary scatterer. From this, a form-free

volume-weighted scaling factor distribution is obtained that best describes the experimental data. As with the original McSAS³⁰, a number of independent optimizations are performed to allow the estimation of the uncertainty of the resulting distribution.

II.E. CDEF vs. the SPONGE vs. other methods

Since the SPONGE has already proven to successfully simulate helicoidal supramolecular copolymers at different structural parameters¹⁸, it is used here to verify the accuracy of the much faster CDEF in order to use the latter with trust. In contrast to the SPONGE, Debyer simplifies computations by binning the distance distribution, thus reducing computational effort at the expense of a less accurate calculation.

Besides binning of the intra-pair distances, which is the most costly calculation step, CDEF employs a quasi-random filling compared to the true random filling as used by the SPONGE. As a result, a smaller number of punctiform scatterers can be used w.r.t. the same usable q -range (section II.C) which reduces computational effort again. A very similar procedure has been introduced by S. Hansen, calculating $I(q)$ of complex-shaped fibrinogen using the distance distribution function of a corresponding quasi-random point cloud¹⁹, without rebinning the distance distribution however. Moreover, Hansen focuses on calculating single-particle $I(q)$ and did not consider polydisperse particles. CDEF additionally allows to adjust the form factors of the individual scattering points, leading to much more versatile applications in case of core-shell-structured particles.

Since CDEF and the SPONGE use an artificial random filling instead of using the exact atomic positions of the particle, computational time is clearly reduced with both methods. For the evaluation of Au nanocubes with face-to-face distance of 50 nm, e.g. choosing 30 000 scatterers instead of $\sim 5.2 \cdot 10^6$ which is the approximate number of atoms in a gold crystallite of this size³¹, the computational effort decreases by a factor of $\approx 30\,500$. The computation of a single SAXS profile using CDEF with 30 000 scatterers requires ≈ 1 s on a single modern desktop computer with a quad core processor. Hence, this would need more than 8 hours in case of $5.2 \cdot 10^6$ scatterers, which justifies the simplification using the quasi-random filling instead of the true atom positions.

For SAXS on isotropic macromolecules, similar approaches of calculating $I(q)$ from the scattering properties of the underlying (atomic) structure have been made in the past by the European Molecular Biology Laboratory (EMBL) by introducing CRY SOL or DAMMIN which are part of the ATSAS software package³²⁻³⁴. In contrast to CDEF however, CRY SOL calculates $I(q)$ of macromolecules in dilute solution from the *exact* crystallographic positions and form factors of their individual atoms³³ which principally is similar to the intended usage of the Debyer software package. In doing so, spherical averaging of the interference terms is done by introduc-

ing spherical harmonics and using their properties of orthogonality to obtain a simplified expression of the total molecular form factor. Since CRY SOL also takes into account scattering from the missing water molecules and the hydration shell of the molecules as correction terms for the molecules' total form factor, it can resolve scattering profiles up to $q \leq 4 \text{ nm}^{-1}$. Despite the higher q -range, using the *exact* crystallographic positions is not suitable to compute $I(q)$ of suspended nanoparticles simply because it would be computationally very intensive since nanoparticles have much bigger sizes and are not as single-particle as macromolecules³³.

II.F. CDEF: Diverse models of cubic particles

To show the versatile application of CDEF, we want to characterize Au nanocubes which are described in section III. In doing so, we implemented three different cubic models (ideal cube, cube with truncated/rounded edges) carrying a homogeneous electron density (fig. 6).

To simulate truncated edges, an algorithm based on the Hessian normal form is implemented with which the truncation-level of the cubic model with a side-to-side distance L can be adjusted. The Hessian normal form describes the shortest distance D of a point with the Euclidean position \vec{x} relative to a given plane described by a support vector \vec{a} and normal vector \vec{n} :

$$D = (\vec{x} - \vec{a}) \cdot \vec{n}. \quad (16)$$

For each scattering point with position \vec{x} , D is calculated for each of the 12 sectional planes which cut the edges of the cubic model (fig. 6). If $D < 0$ for all 12 sectional planes, the point is located inside the cube, because the defined normal vectors \vec{n} are pointing away from the cloud's center by definition. All outside points are deleted by setting their corresponding form factor to zero. The degree of truncation can be influenced by equally varying the length of all \vec{a} by modifying an introduced (truncation) factor T , with

$$\vec{a} = T \frac{L}{\sqrt{2}} \vec{n}. \quad (17)$$

With this definition, $T = 1$ indicates no truncation and corresponds to the *ideal* cube. Furthermore, a cubic model with rounded edges is generated by introducing four cylinders for each Euclidean direction x, y, z whereas each cylinder is located in one of the four corners with its axis being aligned along the corresponding edge (fig. 6). The rounded edges are now generated by deleting points located at the edges and outside of each cylinder. All 12 cylinders are described by the same radius of curvature R_{curve} .

III. SYNTHESIS OF AU NANOCUBES

Mono-crystalline Au nanocubes (fig. 7) were prepared by colloidal chemistry in aqueous solution, according to an already published protocol^{15,35}, in presence of cetyltrimethylammonium bromide (CTAB) as the capping agent. Crystal growth is achieved by chemical reduction of Au⁺ ions on the surface of a gold seed (a small sphere with an initial size of 2 to 3 nm in diameter), resulting in the formation of a cubic shape³⁶. The side length of these particles as determined from SEM images amounts to 55 nm with a standard deviation of 2 nm. Using this particular synthesis procedure leads to a percentage of $\sim 90\%$ of nanocubes w. r. t. the whole particle ensemble and a small amount $\sim 10\%$ of particles with different shapes (see marked spots in fig. 7). The edges and corners of the cubes tend to gradually round out over time. In solution, this phenomenon is slow (6 months), however, it is faster (1 month) when the cubes are deposited on a substrate and kept in air. From the SEM images, a curvature radius ($R_{\text{curve}} \approx 7 \text{ nm}$) was determined for the edges.

IV. EXPERIMENTAL DETAILS

Since the SAXS experiments were conducted in vacuum, the diluted colloidal solution of Au nanocubes suspended in water was filled into a rectangular capillary of borosilicate glass with a homogeneous thickness along its vertical axis, and sealed with a blow torch before measurement. The sample was then loaded into the experimental vacuum chamber which is connected to the four-crystal monochromator (FCM) beamline of the PTB laboratory at the synchrotron radiation facility Bessy II, Berlin. For the experiment, X-ray photons are generated by a bending magnet, and then guided by the beamline to the sample holder resulting in a thin X-ray beam with a cross-sectional area of approximately $150 \mu\text{m} \times 400 \mu\text{m}$ at the samples' position. The FCM-beamline allows to perform experiments in a wide range of photon energies from $E_{\text{ph}} = 1.75 \text{ keV}$ to 10 keV ³⁷. Our SAXS experiments were performed at $E_{\text{ph}} = 8 \text{ keV}$ using the Si (1, 1, 1) monochromator crystals with a spectral resolving power of $E_{\text{ph}} / \Delta E_{\text{ph}} = 10^4$ and a photon flux in the range of $\Phi \approx 10^{10} / \text{s}$ ³⁷. During the experiment, the capillaries were measured at different y -positions along the vertical axis. At each y -position, SAXS images were recorded by a vacuum-compatible PILATUS 1M hybrid-pixel detector with a pixel size of $p = 172 \mu\text{m}$ ³⁸.

IV.A. Data processing

Prior to data evaluation, the two dimensional (2D) SAXS image, consisting of concentric circles, is converted into the corresponding one dimensional SAXS profile in absolute units. This allows us to determine the number concentration of suspended particles. For each distinct y -position, I_{EXP} is circularly integrated around the center

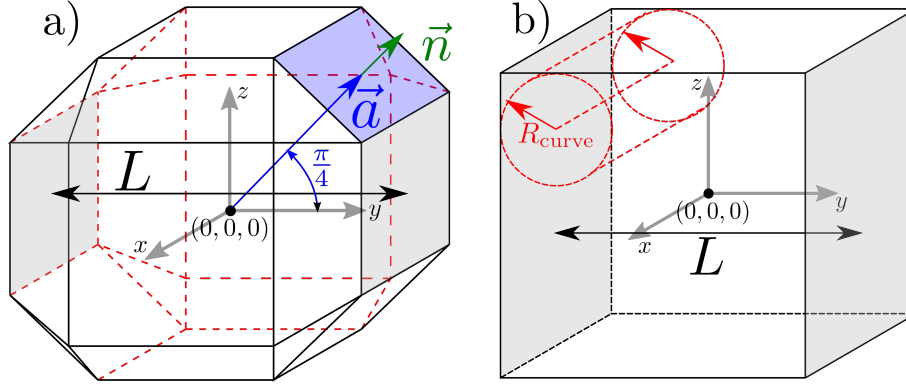


Figure 6 Two different cubic models with face-to-face-distance L . a) Cube with truncated edges. All 12 edges are truncated by sectional planes. Each sectional plane, marked blue, is defined by a support vector \vec{a} , and a normal vector \vec{n} which stands perpendicular on the plane. b) Cube with implied rounded edges. The curve of each edge is defined by identical cylinders with curvature radius R which touch the associated cubic sides.

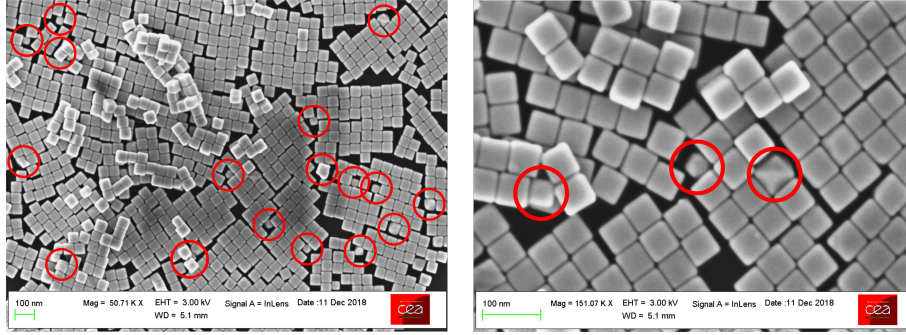


Figure 7 Scanning electron microscopy images of Au nanocubes at two different scales. The population also consists of particles with a non-cubic shape (some marked by red circles).

of the incident beam and then normalized to the incident photon flux, the duration of exposure, the sample thickness and the quantum efficiency of the detector at a given photon energy⁵. Then I_{EXP} is expressed in terms of the momentum transfer q :

$$q = \frac{4\pi E_{\text{ph}}}{hc} \sin\left(\frac{1}{2} \arctan \frac{np}{L}\right) \approx \frac{4\pi E_{\text{ph}}}{hc} \frac{np}{L}, \quad (18)$$

where L is the distance from the sample to the detector plane, n is the number of pixels, and p is the pixel size. Data processing at PTB, up to this point, is standardized using particular in-house software.

Since scattering from water molecules and the walls of the glass capillary is also detected by the SAXS measurement leading to an unwanted background signal, an additional capillary only filled with distilled water was measured during the same measurement to detect the corresponding background curve by which I_{EXP} was eventually subtracted. For better statistics, however, I_{EXP} as well as the background curves were averaged over all y -positions before subtraction.

V. RESULTS AND DISCUSSION

In this section, we present the analysis of Au nanocubes using different cubic models, namely an *ideal* cube, a cube with truncated edges as well as a cube with rounded edges. During the fitting of a shape with varying geometry, such as the truncated cubic model, it is necessary to recalculate the individual single-particle scattering profile I_{MONO} in each step. For steady particle shapes with size changes only, such as ideal cubes, it is sufficient to calculate I_{MONO} once, and then rescale it in accordance to the assumed size distribution.

For all introduced cubic models, the results of the (faster) CDEF are eventually compared to those of the SPONGE in order to confirm the results of CDEF. Figures 11, 12 and 13 compare the volume-weighted size distribution from the SPONGE with the size distribution from CDEF, converted into volume weight. In doing so, both methods evaluated the same experimental data. Since the SPONGE cannot fit shape parameters due to the time-taking computing process, stl-files of CDEF's best-fit particle shapes were generated and then given to the SPONGE to reveal the underlying uncertainty of I_{FIT} .

Using CDEF, each model was fitted to the experimental data by varying the M free parameters, namely the

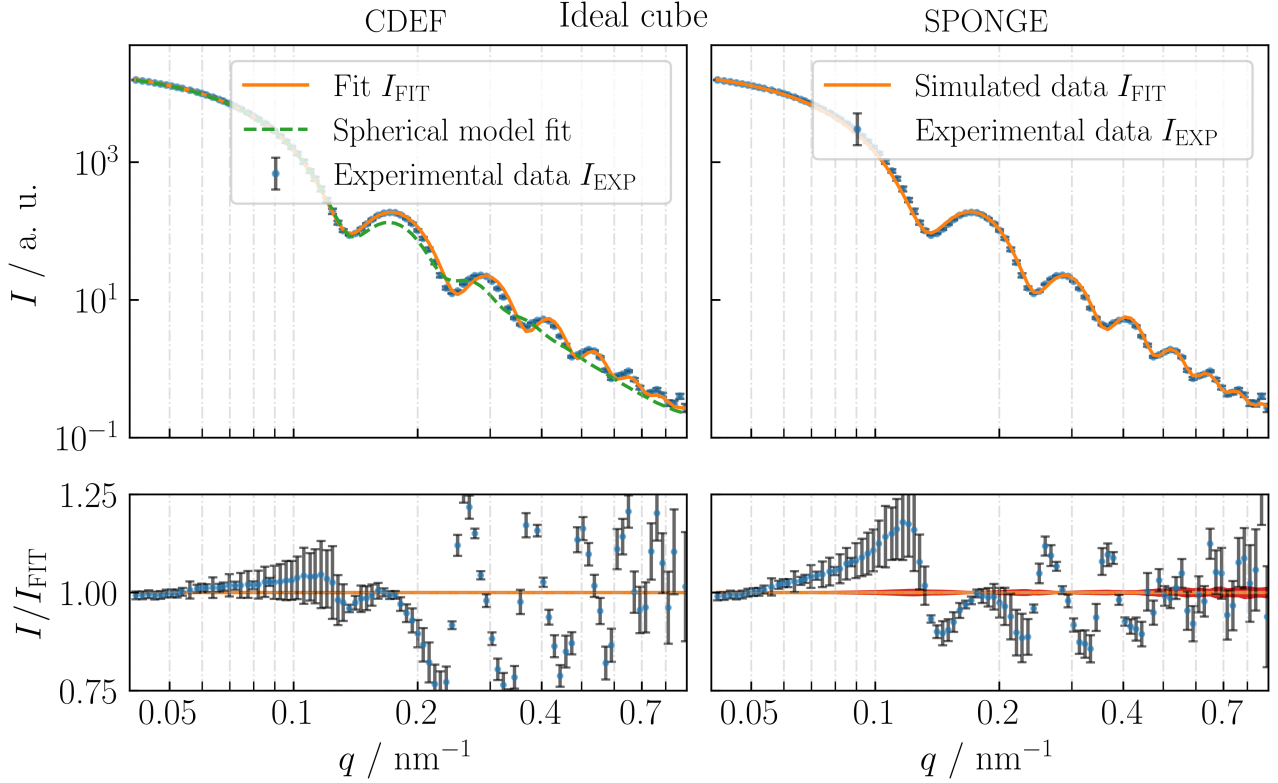


Figure 8 CDEF versus the SPONGE. Fit results of Au nanocubes using the model of an ideal cube. Coupling of the SPONGE with MCSAS additionally reveals an uncertainty of I_{FIT} marked in red the SPONGE's I/I_{FIT} -Plot, thus an uncertainty of the underlying size distribution can be stated (fig. 11). See table I for further information.

number-weighted distribution of the side-to-side length L , which was assumed to be Gaussian, and the truncation or rounding parameters for the imperfect cubes. Powell's algorithm³⁹ with a maximal number of $M \cdot 1000$ function evaluations was used to minimize χ^2 . The combined SPONGE+McSAS was not confined to any particular size distribution, but rather fitted the volume-weighted size distribution numerically.

With CDEF, each 3D cloud initially consisted of $N = 30\,000$ scattering points whereas for each function evaluation step N varied based on the underlying spatial distribution of scatterers, the level of truncation T or radius of curvature R_{curve} such that $N < 30\,000$. This initial number of $N = 30\,000$ was a good compromise to fit the whole q -interval of the experimental data without experiencing any artifacts arising from the clouds' fine structure, but staying below a computing duration of < 4 s per evaluation of χ^2 .

For comparison, a spherical model was additionally included in the evaluation as depicted in fig. 8. The weak match between experimental data and spherical fit demonstrates the sensitivity of the scattering experiment to the particle shape. Even though the ideal cubic model also leads to pronounced deviations at $0.2 \text{ nm}^{-1} < q$, in general it matches the oscillations with better agreement compared to the spherical model which is also confirmed by the corresponding values of χ^2 in table I. The spher-

ical model only matches the Guinier region satisfyingly resulting in a mean diameter of $d = 65.5 \text{ nm}$ with a standard deviation of $\sigma_d = 6.7 \text{ nm}$.

Using the ideal cubic model reveals a volume-weighted mean face-to-face-distance of $L = 52.5 \text{ nm}$ with a distribution width of $\sigma_L = 2.8 \text{ nm}$. With the SPONGE we get an mean value of $L = (53.20 \pm 0.06) \text{ nm}$ with a distribution width of $\sigma_L = (2.7 \pm 1.0) \text{ nm}$ which leads to a relative deviation of $\Delta L / L \approx 1.5 \%$ between CDEF and the SPONGE. Regarding the Guinier region, CDEF seems to give a slightly better fit compared to the SPONGE, whereas in the Porod region the SPONGE is superior.

For both methods, the cubic models with truncated (fig. 9) or rounded edges (fig. 10) fit the experimental data slightly better than the ideal cube. The lower values of χ^2 (table I) also imply a higher degree of compliance for these models which coincides with the fact that the particles' edges and corner gradually round out over time when being stored in suspension above 6 months. The truncated cubic model reveals a mean value of $L = 53.4 \text{ nm}$ with $\sigma_L = 3.3 \text{ nm}$, and a truncation factor of $T = 0.91$. From a geometrical perspective, this truncation factor means that on average $\sim 2.6 \text{ nm}$ are cut off on both sides of each edge. With the SPONGE we obtain a value of $L = (54.00 \pm 0.04) \text{ nm}$ with a distribution width of $\sigma_L = (3.0 \pm 0.8) \text{ nm}$ is obtained. A reason for the relative deviation of $\Delta L / L \approx 1.1 \%$ between CDEF

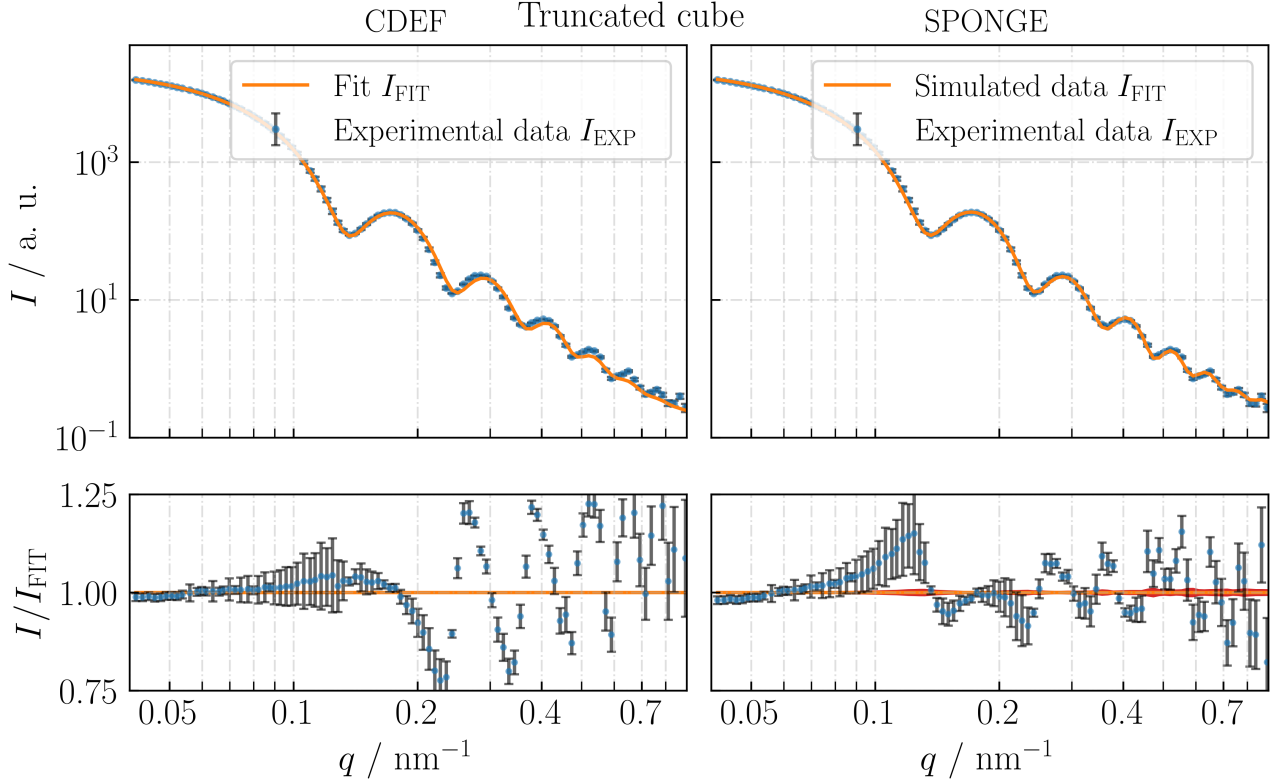


Figure 9 CDEF versus the SPONGE. Fit results of Au nanocubes using a cubic model with truncated edges. Coupling of the SPONGE with MCSAS additionally reveals an uncertainty of I_{FIT} marked in red as explained in fig. 8, thus an uncertainty of the underlying size distribution can be stated (fig. 12)

and the SPONGE (as for the other cubic models) may result from the fact that CDEF is confined to a Gaussian size distribution, whereas the SPONGE is not. This assumption is also confirmed by the fact that there are no deviations in the corresponding single-particle and poly-disperse scattering profiles when comparing CDEF with the SPONGE.

For the model with rounded edges we obtain the same result of $L = 53.4 \text{ nm}$ with $\sigma_L = 3.2 \text{ nm}$. With this model, we additionally obtain a radius of curvature of $R_{\text{curve}} \approx 7 \text{ nm}$ which is in good agreement with the value measured with SEM (section III). With the SPONGE we obtain $L = (54.00 \pm 0.06) \text{ nm}$ and $\sigma_L = (3.1 \pm 0.9) \text{ nm}$. The relative deviation of the mean face-to-face-distance $\Delta L / L$ again equals 1.1 %.

Since the measured ensemble of Au nanocubes does not only consist of cubes with a single shape (ideal, truncated, or rounded), but partially contains all of them plus particles with undefined (i.e. non-cubic) shapes (fig. 7), none of the specific cubic models used is actually able to exactly fit the measurement data, meaning $I/I_{\text{FIT}} \approx 1$ for the entire q -range, respectively $\chi^2 \leq 1$. Also the uncertainty estimate coming from data processing (chapter IV.A), meaning the background subtraction in particular, could be underestimated.

Thus, a next step to improve the overall model of the particle ensemble could be the application of a model

function including all assumed cubic models with their volume-weighted percentage of the total particle population. The percentage would need to be determined for a representative sample of the ensemble in advance, for instance using microscopic methods with which number-weighted percentages would be obtained.

VI. CONCLUSION

CDEF is suitable to calculate single-particle SAXS profiles of common particle shapes (excluding cylinders with aspect ratios above ~ 4) with satisfying accuracy which was shown by comparison with known analytic form factors. Here, a sufficient but minimal number of scattering points should be selected though in order to prevent artifacts from appearing in the scattering profile but keeping computing effort low. Occasional cross-checks can be made between CDEF and the SPONGE to ensure the speed improving assumptions in CDEF are not interfering with the accuracy of the results. Using CDEF, polydisperse SAXS pattern can also be generated, eventually allowing experimental data to be evaluated. For all presented cubic models, a direct comparison between CDEF and the SPONGE concerning the size distribution of Au nanocubes reveals good agreement between results, with a deviation of the mean size of $\leq 1.5 \%$, even though CDEF uses the histogram approximation

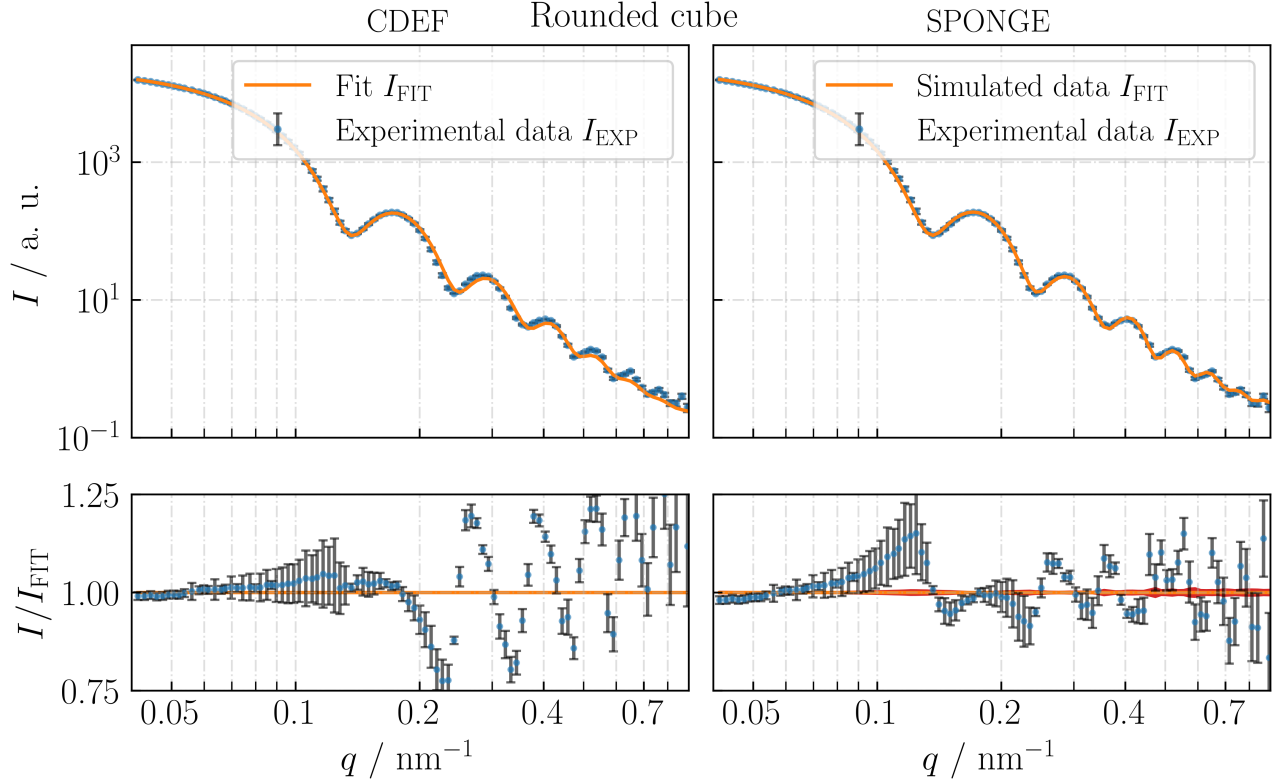


Figure 10 CDEF versus the SPONGE. Fit results of Au nanocubes using a cubic model with truncated edges. Coupling of the SPONGE with MCSAS additionally reveals an uncertainty of I_{FIT} , thus an uncertainty of the underlying size distribution can be stated (fig. 13). See table I for further information.

Table I CDEF: Summary of fitting results of homogeneous cubic models with fitting prefactor N_C , mean particle size L , standard deviation σ_L , truncation factor T (in terms of $L/\sqrt{2}$), radius of curvature R_{curve} (in terms of $L/2$), number of iterations N_{iter} of Powell algorithm, number of function evaluations N_{fev} of function χ^2 and computing time t .

Model	C^a / cm^{-3}	L / nm	σ_L / nm	$T / 1$	$R_{\text{curve}} / 1$	χ^2	N_{iter}	N_{fev}	t / s
Ideal cube	$8.709 \cdot 10^9$	52.5	2.8	0.91	0.27 (7.2 nm)	< 33	5	262	< 37
Truncated cube	$8.604 \cdot 10^9$	53.4	3.3			< 23	5	433	< 1339
Rounded cube	$8.562 \cdot 10^9$	53.4	3.3			< 21	6	493	< 1172
Sphere	$8.636 \cdot 10^9$	31.7 ^b	3.4 ^c			< 158	5	274	< 39

^aNumber concentration is based on an electron contrast of $\Delta\rho \approx 4077 \text{ nm}^{-3}$ of Au-particles suspended in H_2O at 8 keV.

^bSpherical radius in nm.

^cStandard deviation of radius in nm.

of the point-pair distances through Debye and is confined to a Gaussian distribution. On the other hand, the coupling of the SPONGE with McSAS3 allows the determination of size distributions of odd-shaped particles when no information on the shape of the analytical size distribution is known. This time-saving approach of implementing Debye's scattering equation for SAXS allows to introduce further fit parameters to modify the average particle shape, thus enabling the user to gain more detailed information of the measured nanoparticles. The approach can potentially be extended to include core-shell morphologies by varying the density of scatterers or assigning different electron densities to the individual punctiform scatterers. Further speed-up could be achieved by an implementation which runs on parallel

hardware such as consumer graphics cards.

ACKNOWLEDGMENTS

This work was partly funded by the 17NRM04 nP-Size project of the EMPIR programme co-financed by the EMPIR participating states and by the European Union's Horizon 2020 research and innovation programme.

Finally, we want to thank Levent Cibik and Jan Weser from PTB for their help constructing different particle shapes using CAD as well as for their beamline support.

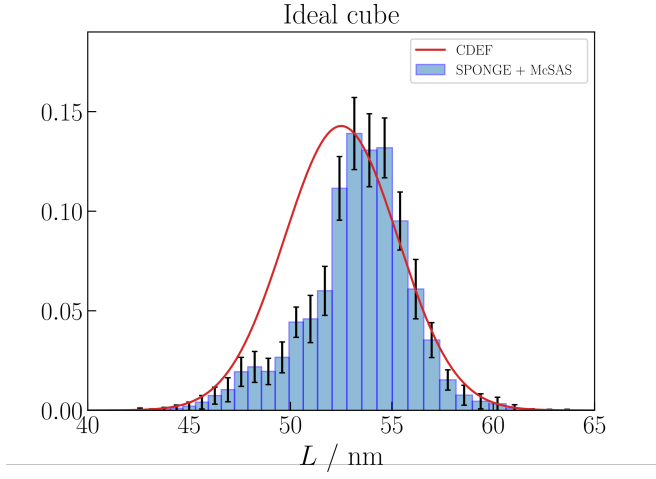


Figure 11 CDEF vs. the SPONGE: Normalized distribution of side-to-side length of the Au nanocubes. The uncertainty of the volume-weighted distribution using the SPONGE with a mean value of $L = (53.20 \pm 0.06)$ nm is indicated by error bars. The volume-weighted distribution using CDEF reveals a mean value of $L = 52.5$ nm.

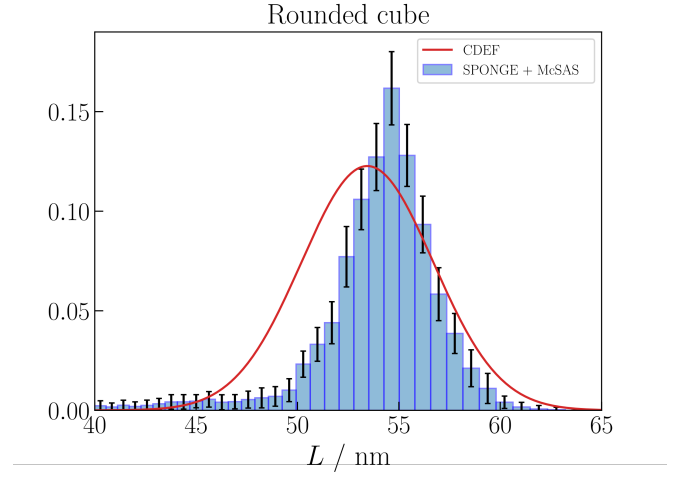


Figure 13 CDEF vs. the SPONGE: the SPONGE's volume-weighted size distribution reveals a mean value of $L = (54.00 \pm 0.06)$ nm. The volume-weighted distribution using CDEF again shows an expectation value of $L = 53.4$ nm.

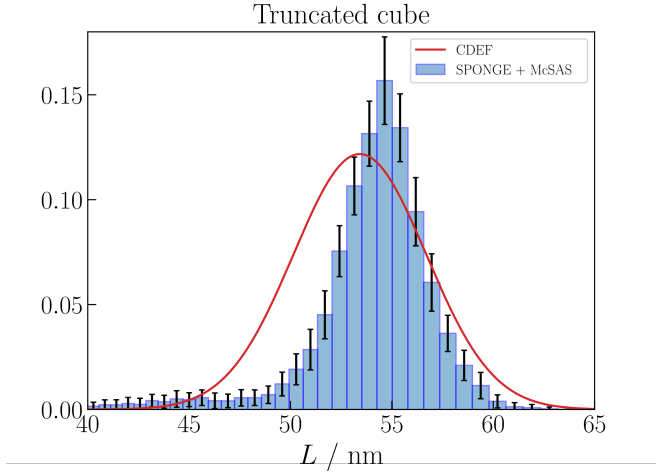


Figure 12 CDEF vs. the SPONGE: the SPONGE's volume-weighted size distribution reveals a mean value of $L = (54.00 \pm 0.04)$ nm. The volume-weighted distribution using CDEF shows an expectation value of $L = 53.4$ nm.

REFERENCES

- ^{*}) Electronic mail: jerome.deumer@ptb.de
- [†]) Electronic mail: Brian.Pauw@bam.de
- [‡]) Electronic mail: sylvie.marguet@cea.fr
- [§]) Electronic mail: dieter.skroblin@ptb.de
- [¶]) Electronic mail: olivier.tache@cea.fr
- ^{||}) Electronic mail: michael.krumrey@ptb.de
- ^{**}) Electronic mail: christian.gollwitzer@ptb.de
- ¹ André Guinier and Gérard Fournet. *Small-Angle Scattering of X-rays*. John Wiley & Son, Inc., 1955.
 - ² O. Glatter and O. Kratky, editors. *Small Angle X-ray Scattering*. ACADEMIC PRESS INC. (LONDON) LTD., 1982.
 - ³ Joachim Kohlbrecher. *User guide for the SASfit software package*. Paul Scherrer Institute, 2020.
 - ⁴ Raul Garcia-Diez, Aneta Sikora, Christian Gollwitzer, Caterina Minelli, and Michael Krumrey. Simultaneous size and density determination of polymeric colloids by continuous contrast variation in small angle X-ray scattering. *European Polymer Journal*, 81:641–649, 2016.
 - ⁵ Alexander Schavkan, Christian Gollwitzer, Raul Garcia-Diez, Michael Krumrey, Caterina Minelli, Dorota Bartczak, Susana Cuello-Núñez, Heidi Goenaga-Infante, Jenny Rissler, Eva Sjöström, Guillaume Baur, Konstantina Vasilatou, and Alexander Shard. Number Concentration of Gold Nanoparticles in Suspension: SAXS and spICPMS as Traceable Methods Compared to Laboratory Methods. *Nanomaterials*, 9:502, 2019.
 - ⁶ Christian Gollwitzer, Dorota Bartczak, Heidi Goenaga-Infante, Vikram Kestens, Michael Krumrey, Caterina Minelli, Marcell Pálmai, Yannic Ramaye, Gert Roebben, Aneta Sikora, and Zoltán Varga. A comparison of techniques for size measurement of nanoparticles in cell culture medium. *Analytical Methods*, 8(26):5272–5282, 2016.
 - ⁷ V. Bock, A. Emmerling, R. Saliger, and J. Fricke. Structural Investigation of Resorcinol Formaldehyde and Carbon Aerogels Using SAXS and BET. *Journal of Porous Materials*, 4:287–294, 1997.
 - ⁸ Jan Skov Pedersen. *Neutrons, X-Rays and Light. Scattering Methods Applied to Soft Condensed Matter*, chapter 16 - Modelling of Small-Angle Scattering Data from Colloids and Polymer Systems, page 552. Elsevier Science B.V., 2002.
 - ⁹ Raul Garcia-Diez, Christian Gollwitzer, and Michael Krumrey. Nanoparticle characterization by continuous contrast variation in SAXS with a solvent density gradient. *Journal of Applied Crystallography*, 48(1):20–28, 2015.
 - ¹⁰ Luciano Galantini, Edoardo Giglio, Antonio Leonelli, and Nicolae Viorel Pavel. An Integrated Study of Small-Angle X-ray Scattering and Dynamic Light Scattering on Cylindrical Micelles of Sodium Glycodyoxycholate. *The Journal of Physical Chemistry B*, 108:3078–3085, 2004.
 - ¹¹ Konstantin A. Shapovalov. Light Scattering by a Prism and Pyramid in the Rayleigh-Gans-Debye Approximation. *Optics*, 2:32–37, 2013.
 - ¹² Roman Nayuk and Klaus Huber. Formfactors of Hollow and Massive Rectangular Parallelepipeds at Variable Degree of Anisotropy. *Zeitschrift für Physikalische Chemie*, 226:837–854, 2012.
 - ¹³ Artur Feld, Agnes Weimer, Andreas Kornowski, Naomi Winkelmann, Jan-Philip Merkl, Hauke Kloust, Robert Zierold, Christian Schmidtke, Theo Schotten, Maria Riedner, Sara Bals, and Horst Weller. Chemistry of Shape-Controlled Iron Oxide Nanocrystal Formation. *ACS Nano*, 13:152–162, 2019.
 - ¹⁴ Zijian Zhou, Xianglong Zhu, Dongjun Wu, Qiaoli Chen, Dengtong Huang, Chengjie Sun, Jingyu Xin, Kaiyuan Ni, and Jinhao Gao. Anisotropic Shaped Iron Oxide Nanostructures: Controlled Synthesis and Proton Relaxation Shortening Effects. *Chemistry of Materials*, 27:3505–3515, 2015.
 - ¹⁵ Mohamed Haggui, Montacer Dridi, Jerome Plain, Sylvie Marguet, Henri Perez, George C. Schatz, Gary P. Wiederrecht, Stephen K. Gray, and Renaud Bachelot. Spatial Confinement of Electromagnetic Hot and Cold Spots in Gold Nanocubes. *ACS Nano*, 2:1299–1307, 2012.
 - ¹⁶ Ingo Breßler, Joachim Kohlbrecher, and Andreas F. Thünemann. *SASfit* : a tool for small-angle scattering data analysis using a library of analytical expressions. *Journal of Applied Crystallography*, 48:1587–1598, 2015.
 - ¹⁷ SasView - SasView for Small Angle Scattering Analysis, 2021.
 - ¹⁸ Keisuke Aratsu, Rika Takeya, Brian R. Pauw, Martin J. Holamby, Yuichi Kitamoto, Nobutaka Shimizu, Hideaki Takagi, Rie Haruki, Shin-ichi Adachi, and Shiki Yagai. Supramolecular copolymerization driven by integrative self-sorting of hydrogen-bonded rosettes. *nature communications*, 11(1):1623, 2020.
 - ¹⁹ Steen Hansen. Calculation of small-angle scattering profiles using Monte Carlo simulation. *Journal of Applied Crystallography*, 23:344–346, 1990.
 - ²⁰ Debye software package, 2020.
 - ²¹ Christopher L. Farrow and Simon J. L. Billinge. Relationship between the atomic pair distribution function and the small-angle scattering: implications for modeling of nanoparticles. *Acta Crystallographica Section A*, 65:232–239, 2009.
 - ²² Harald Ibach and Hans Lüth. *Festkörperphysik*. Springer, 2008.
 - ²³ Peter Debye. Zerstreuung von Röntgenstrahlen. *Annalen der Physik*, 351:809–823, 1915.
 - ²⁴ Bart Vandewoestyne and Ronald Cools. Good permutations for deterministic scrambled Halton sequences in terms of L2-discrepancy. *Journal of Computational and Applied Mathematics*, 189(1-2):341–361, 2006.
 - ²⁵ Philip R. Bevington and D. Keith Robinson. *Data Reduction and Error Analysis for the Physical Science*. Peteron, Kent A., 3 edition, 2003.
 - ²⁶ SciPy v1.6.1. *Reference Guide - Spatial algorithms and data structures*, 2021.
 - ²⁷ Brian R. Pauw, Jan Skov Pedersen, Samuel Tardif, Takata Masaki, and Bo B. Iversen. Improvements and considerations for size distribution retrieval from small-angle scattering data by Monte Carlo methods. *Journal of Applied Crystallography*, 46:365–371, 2013.
 - ²⁸ I. Bressler, B. R. Pauw, and A. F. Thünemann. McSAS: software for the retrieval of model parameter distributions from scattering patterns. *Journal of Applied Crystallography*, 48:962–969, 2015.
 - ²⁹ Ingo Breßler. Github: BAMresearch / McSAS. Online, 2017.
 - ³⁰ Brian Richard Pauw, Jan-Skov Pedersen, Samuel Tardif, Masaki Takata, and Bo Brummersted Iversen. Improvements and considerations for size distribution retrieval from small-angle scattering data by monte-carlo methods. *Journal of Applied Crystallography*, 46:365–371, 2003.
 - ³¹ Linus Pauling. Atomic Radii and Interatomic Distances in Metals. *Journal of the American Chemical Society*, 69(3):542–553, 1947.
 - ³² D. Franke, M. V. Petoukhov, P. V. Konarev, A. Panjkovic, A. Tuukkanen, H. D. T. Mertens, A. G. Kikhney, N. R. Hajizadeh, J. M. Franklin, C. M. Jeffries, and D. I. Svergun. AT-SAS 2.8: a comprehensive data analysis suite for small-angle scattering from macromolecular solutions. *Journal of Applied Crystallography*, 50:1212–1225, 2017.
 - ³³ D. Svergun, C. Barberato, and M. H. J. Koch. CRY SOL-a Program to Evaluate X-ray Solution Scattering of Biological Macromolecules from Atomic Coordinates. *Journal of Applied Crystallography*, 28:768–773, 1995.
 - ³⁴ D. I. Svergun. Restoring Low Resolution Structure of Biological Macromolecules from Solution Scattering Using Simulated Annealing. *Biophysical Journal*, 76:2879–2886, 1999.
 - ³⁵ Farid Kameche, Wajdi Heni, Siham Telitel, Dandan Ge, Loic Vidal, Frédéric Dumur, Didier Gimes, Jacques Lalevée, Sylvie Marguet, Ludovic Douillard, Céline Fiorini-Debuisschert, Renaud Bachelot, and Olivier Soppera. Plasmon-triggered living photopolymerization for elaboration of hybrid polymer/metal nanoparticles. *Elsevier - Materials Today*, 40:38–47, 2020.
 - ³⁶ Bing-Hong Kuo, Chi-Fu Hsia, Tzu-Ning Chen, and Michael H. Huang. Systematic Shape Evolution of Gold Nanocrystals Achieved through Adjustment in the Amount of H₂SO₄ Solution Used. *The Journal of Physical Chemistry C*, 122:25118–25126, 2018.
 - ³⁷ Michael Krumrey. Design of a Four-Crystal Monochromator Beamline for Radiometry at BESSY II. *Journal of Synchrotron Radiation*, 5(1):6–9, 1998.

- ³⁸Jan Wernecke, Christian Gollwitzer, Peter Müller, and Michael Krumrey. Characterization of an in-vacuum PILATUS 1M detector. *Journal of Synchrotron Radiation*, 83:83–90, 2014.
- ³⁹Roger Fletcher and Michael J. D. Powell. A rapidly convergent descent method for minimization. *Oxford University Press - The Computer Journal*, 6:163–168, 1963.
- ⁴⁰Donald E. Knuth. *The TeXbook*. Addison-Wesley, 1984.
- ⁴¹Leslie Lamport. *L^AT_EX: A Document Preparation System*. Addison-Wesley, 1986.
- ⁴²L. Pauling. Icosahedral quasicrystals of intermetallic compounds are icosahedral twins of cubic crystals of three kinds, consisting of large (about 5000 atoms) icosahedral complexes in either a cubic body-centered or a cubic face-centered arrangement or smaller (about 1350 atoms) icosahedral complexes in the β -tungsten arrangement. *Proc. Natl Acad. Sci USA*, 86:8595–8599, 1989.
- ⁴³E. Parthé and L.M. Gelato. The standardization of inorganic crystal-structure data. *Acta Cryst.*, A40:169–183, 1984.
- ⁴⁴D. Rauch, H. & Petrascheck. Grundlagen für ein laue-neutroneninterferometer teil 1: Dynamische beugung. Report AIAU 74405b, Atominstitut der Österreichischen Universitäten, Austria, 1976.
- ⁴⁵J. A. Nelder and R. Mead. A Simplex Method for Function Minimization. *The Computer Journal*, 7(4):308–313, 1965.
- ⁴⁶Armin Hoell, Zoltan Varga, Vikram Singh Raghuvanshi, Michael Krumrey, Christian Bocker, and Christian Rüssel. ASAXS study of CaF₂ nanoparticles embedded in a silicate glass matrix. *Journal of Applied Crystallography*, 47(1):60–66, 2014.
- ⁴⁷Brian Richard Pauw. Everything SAXS: small-angle scattering pattern collection and correction. *Journal of Physics: Condensed Matter*, 25(38):38321, 2013.
- ⁴⁸Mika Pflüger, Victor Soltwisch, Jürgen Probst, Frank Scholze, and Michael Krumrey. Grazing-incidence small-angle X-ray scattering (GISAXS) on small periodic targets using large beams. *IUCrJ*, 4(4):431–438, 2017.
- ⁴⁹M. Krumrey and G. Ulm. High-accuracy detector calibration at the PTB four-crystal monochromator beamline. *Nuclear Instruments and Methods in Physics Research Section A: Accelerators, Spectrometers, Detectors and Associated Equipment*, 467-468:1175–1178, 2001.
- ⁵⁰Albert Thompson, David Attwood, Eric Gullikson, Malcolm Howells, and Kwang-Je Kim. X-RAY DATA BOOKLET, 2009.
- ⁵¹Jeong-Eun Park, Yeonhee Lee, and Jwa-Min Nam. Precisely Shaped, Uniformly Formed Gold Nanocubes with Ultrahigh Reproducibility in Single-Particle Scattering and Surface-Enhanced Raman Scattering. *Nano Letters*, 18:6475–6482, 2018.
- ⁵²O. Glatter. Evaluation of Small-Angle Scattering Data from Lemellar and Cylindrical Particles by the Indirect Transformation Method. *Journal of Applied Crystallography*, 13:577–584, 1980.
- ⁵³Matija Tomsic, Fritz-Popovski, Lukas Vlcek, and Andrej Jamnik. Calculating Small-Angle X-Ray Scattering Intensities from Monte Carlo Results: Exploring Different Approaches on the Example of Primary Alcohols. *Acta Chimica Slovenica*, 54(3):484–491, 2007.